Studying dark matter haloes with weak lensing

Velander, M.B.M.

2 A new shape measurement method and its application to galaxies with colour gradients in weak lensing surveys

Sections to be published in Semboloni E., Velander M., Hoekstra H., Kuijken K., et al, in preparation

As one of the most powerful probes of cosmology, weak gravitational lensing is now the main motivation behind some of the largest near-future optical surveys ever undertaken. The statistical nature of the method requires analysis of a large number of sources, and the minute distortions involved demand high-quality data and precise shape measurements. Weak lensing software therefore has to be both fast and accurate, and such a software suite is introduced and tested in this Chapter. This MV pipeline is shown to be very competitive, with the added benefit of being able to measure higher-order lensing distortions, or flexion. The tests described in this Chapter involve both monochromatic and non-monochromatic simulations, where the latter have been included to assess the amount of bias induced by a wavelength-dependent PSF. Since most galaxies display colour gradients, with a core that has a different colour from the outskirts, a wavelength-dependent PSF will affect different parts of the galaxy image differently. Thus some additional shape bias may be introduced if the PSF is not precisely corrected for. Creating simulations based on real galaxies observed in two different filters, we find that the additional bias induced by this effect is not greater than the bias inherent in the shape measurement software itself. We conclude from our tests that given enough training data we will most likely be able to characterise the colour gradient bias sufficiently accurately to correct for it in future Euclid-like surveys.

2.1 Introduction

With weak gravitational lensing rapidly gaining traction as a powerful probe of cosmology, new surveys are being designed with lensing as a main science goal. Since weak lensing relies on the statistical properties of a galaxy population, large surveys are necessary to minimise systematics such as the intrinsic shape noise. The great number of precise measurements required for future weak lensing analyses increases the necessity for shape measurement software to be both fast and accurate. Currently there is a fair amount of software available, most of which is centred either around the determination of shapes from combinations of weighted second-order brightness moments, such as the method introduced in Kaiser, Squires, & Broadhurst (1995) (KSB hereafter), or around model fitting techniques such as LENSFIT (Miller et al., 2007; Kitching et al., 2008) or Shapelets (Refregier, 2003; Refregier & Bacon, 2003).

The design of a survey also has to take systematics other than those due to biases in shape measurements into account, and primary amongst them is the shape distortion induced by the telescope and, in the case of ground-based surveys, by the atmosphere. This shape distortion is known as the point-spread function (PSF) and can cause coherent distortion across a survey field, biasing the lensing signal. KSB methods have the inherent limitation of too simplistic a description of the PSF and not all realistic PSFs can be accurately accounted for using this description (see e.g. Hoekstra et al., 1998). LENSFIT has a more flexible PSF model and has been proven to be accurate when applied to simulations such as the Gravitational Lensing Accuracy Testing 2008 set (GREAT08; Bridle et al., 2009, 2010), but due to the Bayesian approach it is unfeasibly slow for large near-future surveys. We have therefore chosen to base the new shape measurement software introduced and tested in this Chapter, the MV pipeline, on Shapelets which are both flexible and fast thanks to their analytical nature. Because of their definition as a set of Gauss-Hermite polynomials, any distortion or convolution may be done analytically. This makes it straight-forward to extend the shape analysis to higher-order lensing distortions, known as flexions, without loss of time or accuracy. Flexion, which quantifies variations in shear across a source image, was first discussed in Goldberg & Natarajan (2002) and the notation was then further developed in Goldberg & Bacon (2005) and Bacon et al. (2006). Adding flexion to shear results in a weak arc-like shape which is a better description of the true lensing-induced distortion than the shear stretch alone. Flexion is sensitive to small-scale fluctuations so added detail to mass reconstructions is gained by including it. This makes flexion a powerful complement to shear, particularly for detecting substructure within dark matter haloes (Okura et al., 2008; Bacon et al., 2010; Er et al., 2010; Leonard et al., 2011), or for determining their profiles and shapes (Hawken & Bridle, 2009; Er & Schneider, 2011; Er et al., 2011).

In this Chapter we convey the details of the MV pipeline and the tests performed on it using the GREAT08 simulations and simulations created specifically for the purpose of testing the MV pipeline in preparation for the analysis of space-based data. Both sets of simulations are monochromatic in nature, but recently the question of the impact of a wavelength-dependent PSF on shape measurement accuracy was raised (Voigt et al., 2011). Since the PSF is a function of wavelength, and since galaxies in general are expected to display

different colours in their cores and disks, the PSF will look different at different points on a galaxy image. Thus two galaxies with dissimilar intrinsic shapes and colour gradients may become indistinguishable after being convolved with a wavelength-dependent PSF. Perfectly correcting for the PSF in such a case is impossible without further information on the colour gradient of the galaxy. This could present a challenge for surveys where observations are done using a broad-band filter such as the planned space-based Euclid[1] survey, scheduled for launch in 2019. The ultimate impact of this effect on weak lensing analyses will depend on the true intrinsic colours of the galaxy distribution and on the total shape measurement bias induced by the wavelength-dependent PSF. For the first part several studies into colour gradients of galaxies have been carried out in the context of galaxy evolution, most of them at low redshifts (e.g. Gonzalez-Perez et al., 2011). To assess the impact of the second part, the bias induced by a wavelength-dependent PSF, representative simulations have to be created. In this Chapter we use real galaxies from the All-Wavelength Extended Groth Strip International Survey (AEGIS; Davis et al., 2007) together with photometric redshifts from the third Canada-France-Hawaii Telescope Legacy Survey Deep field (CFHTLS-Deep3) to create realistic broad-band simulations. AEGIS is here assumed to provide a representative galaxy sample which has been observed through two filters with the Advanced Camera for Surveys (ACS) onboard the *Hubble Space Telescope* (HST). These two filters can be combined to approximate the broad-band filter proposed for Euclid and therefore these data form the ideal starting point for Euclid-like simulations. The MV pipeline is then tested on these simulations to determine the level of bias induced by colour gradients in galaxies, and to identify the galaxy properties that have the greatest impact on this bias.

This Chapter is organised as follows: in Section 2.2 we introduce the theoretical background of shear and flexion, and of Shapelets, with the MV pipeline being described in detail in Section 2.2.3. Monochromatic tests of the MV pipeline are carried out in Section 2.3 and the software is applied to non-monochromatic simulations in Section 2.4. We conclude in Section 2.5.

2.2 Theoretical background

2.2.1 Shear and flexion

If the lensing convergence and shear are not constant across a given source image, then we need to quantify how they vary. This can be done by measuring higher-order lensing distortions known as flexion. The formalism was first explored by Goldberg & Bacon (2005) and then further investigated by Bacon et al. (2006) (hereafter B06). In the weak lensing regime where convergence is small the lensed surface brightness of a source galaxy, $f(\mathbf{x})$, and the unlensed surface brightness, $f_0(\mathbf{x})$, are related through

$$f(\mathbf{x}) \simeq \left\{1 + \left[(A-I)_{ij}x_j + \frac{1}{2}D_{ijk}x_jx_k\right]\frac{\partial}{\partial x_i}\right\} f_0(\mathbf{x}). \tag{2.1}$$

where I is the identity matrix, x_i denotes lensed coordinates, and A is a distortion matrix which may be expressed in terms of convergence κ and shear

[1] http://www.euclid-ec.org

γ:

$$\mathrm{A} = \begin{pmatrix} 1-\kappa-\gamma_1 & -\gamma_2 \\ -\gamma_2 & 1-\kappa+\gamma_1 \end{pmatrix}. \tag{2.2}$$

$D_{ijk} \equiv \partial A_{ij}/\partial x_k$ describes how the lensing field varies across a source image. Assuming that there are no such fluctuations, an assumption which may be valid if e.g. the source image is very small, is equivalent to setting $D_{ijk} = 0$. We can now re-express this matrix as a sum of two quantities: $D_{ijk} = \mathcal{F}_{ijk} + \mathcal{G}_{ijk}$. These two quantities are referred to as first flexion, or *F flexion*, and second flexion, or *G flexion*, respectively and similarly to shear have two components each. To make the relation between convergence, shear and flexion clear we can express all quantities in terms of derivatives of the lensing potential ψ (see e.g. Hawken & Bridle, 2009):

$$\kappa = \frac{1}{2}(\psi_{xx} + \psi_{yy}) \tag{2.3}$$

$$\gamma_1 = \frac{1}{2}(\psi_{xx} - \psi_{yy}) \tag{2.4}$$

$$\gamma_2 = \psi_{xy} \tag{2.5}$$

$$\mathcal{F}_1 = \frac{1}{2}(\psi_{xxx} + \psi_{yyx}) \tag{2.6}$$

$$\mathcal{F}_2 = \frac{1}{2}(\psi_{xxy} + \psi_{yyy}) \tag{2.7}$$

$$\mathcal{G}_1 = \frac{1}{2}(\psi_{xxx} - 3\psi_{xyy}) \tag{2.8}$$

$$\mathcal{G}_2 = \frac{1}{2}(3\psi_{xxy} - \psi_{yyy}) \tag{2.9}$$

The full matrices $\mathcal{F}_{ijk}$ and $\mathcal{G}_{ijk}$ in terms of the four flexion components are written explicitly in B06. Visually, if the shear is a stretch in one direction then F flexion is a subtle skewness of the brightness profile reminiscent of a centroid shift and the G flexion has three-fold rotational symmetry. When all the above distortions are applied to a circular object, a weak arc is created.

2.2.2 Shapelets

The shape measurement pipeline presented in this Chapter is based on the Shapelet formalism which makes possible the linear decomposition of a galaxy image with surface brightness $f(\mathbf{x})$ into a set of complete and orthogonal basis functions B_{ab} called Shapelets:

$$f(\mathbf{x}) = \sum_{a=0}^{\infty}\sum_{b=0}^{\infty} s_{ab} B_{ab}(\mathbf{x};\beta) \tag{2.10}$$

where s_{ab} are the Shapelets coefficients. The formalism was first introduced by Refregier (2003) and its application to weak lensing shape estimates was further studied in Refregier & Bacon (2003). The basis functions employed consist of Gauss-Hermite polynomials:

$$B_{ab}(\mathbf{x};\beta) = k_{ab}\beta^{-1} e^{-\frac{|\mathbf{x}|^2}{2\beta^2}} H_a(x/\beta) H_b(y/\beta). \tag{2.11}$$

The Hermite polynomial of order n, H_n, depends on the coordinate on the image plane and on the Shapelets scale radius β, and the basis functions are normalised by a constant k_{ab}. What makes Shapelets powerful is not only their completeness but also their invariance under Fourier transforms which enables us to do convolutions analytically. This makes Shapelets a very fast method for determining distortions which is essential to weak lensing, particularly for dedicated surveys where a large number of objects have to be analysed. They are also analogous to the eigenstates of the two-dimensional quantum harmonic oscillator, and thus any linear transformation such as translation, rotation, dilation and shear and flexion can be expressed as a combination of ladder operators:

$$\hat{a}_i \equiv \frac{1}{\sqrt{2}}(\hat{x}_i + i\hat{p}_i) \tag{2.12}$$

$$\hat{a}_i^\dagger \equiv \frac{1}{\sqrt{2}}(\hat{x}_i - i\hat{p}_i) \tag{2.13}$$

where $i = 1, 2$ (for the x- and y-directions), $\hat{x} \equiv x$ and $\hat{p} \equiv \partial/\partial x$. The property raised or lowered by these operators is known as *spin*; a quantity which is invariant under rotation by an angle $\phi = 2\pi/s$ is said to be a spin-s quantity. Thus shear (or ellipticity) is a spin-2 quantity, while F flexion is spin-1 and G flexion is spin-3. The shear operators may be written in terms of raising and lowering operators as

$$\hat{S}_1 = \frac{1}{2}\left(\hat{a}_1^{\dagger 2} - \hat{a}_2^{\dagger 2} - \hat{a}_1^2 + \hat{a}_2^2\right) \tag{2.14}$$

$$\hat{S}_2 = \hat{a}_1^\dagger \hat{a}_2^\dagger - \hat{a}_1 \hat{a}_2 \tag{2.15}$$

or, in terms of the $\hat{x}$ and $\hat{p}$ operators

$$\hat{S}_1 = -\frac{1}{2}\left(\hat{x}_1\hat{p}_1 - \hat{x}_2\hat{p}_2\right) \tag{2.16}$$

$$\hat{S}_2 = -\frac{1}{2}\left(\hat{x}_1\hat{p}_2 + \hat{x}_2\hat{p}_1\right) \tag{2.17}$$

Using the same notation we can write simple analytical expressions for the flexion operators:

$$\hat{\mathcal{F}}_1 = -\frac{1}{8}\left(3\hat{x}_1^2\hat{p}_1 + 2\hat{x}_1\hat{x}_2\hat{p}_2 + \hat{x}_2^2\hat{p}_1\right) \tag{2.18}$$

$$\hat{\mathcal{F}}_2 = -\frac{1}{8}\left(\hat{x}_1^2\hat{p}_2 + 2\hat{x}_1\hat{x}_2\hat{p}_1 + 3\hat{x}_2^2\hat{p}_2\right) \tag{2.19}$$

$$\hat{\mathcal{G}}_1 = -\frac{1}{8}\left(\hat{x}_1^2\hat{p}_1 - 2\hat{x}_1\hat{x}_2\hat{p}_2 - \hat{x}_2^2\hat{p}_1\right) \tag{2.20}$$

$$\hat{\mathcal{G}}_2 = -\frac{1}{8}\left(\hat{x}_1^2\hat{p}_2 + 2\hat{x}_1\hat{x}_2\hat{p}_1 - \hat{x}_2^2\hat{p}_2\right) \tag{2.21}$$

Applying these operators to circular Shapelets we thus get an image which is 'flexed'.

Using Shapelets, the point-spread function (PSF) can be convolved with a galaxy image in a similarly analytical fashion. The PSF is described by a distortion matrix $\mathbf{P}$:

$$\mathbf{P}_{a_1a_2b_1b_2}(\beta_{\rm obj}, \beta_{\rm con}) = \sum_{a_3,b_3} C_{a_1a_2a_3}^{\beta_{\rm con}\beta_{\rm obj}\beta_{\rm psf}} C_{b_1b_2b_3}^{\beta_{\rm con}\beta_{\rm obj}\beta_{\rm psf}} p_{a_3b_3} \tag{2.22}$$

Here p_{ab} are the Shapelets coefficients of the PSF and $\beta_{\rm psf}$, $\beta_{\rm obj}$ and $\beta_{\rm con}$ are the scale radii of the PSF, the object and the resulting PSF convolved object respectively. $C_{nml}^{\beta_1\beta_2\beta_3}$ is a convolution tensor which depends on the different scale radii. The full expression is given in Refregier (2003). The PSF convolution is then done by multiplying the above matrix and the Shapelets expansion of the object being convolved.

2.2.3 The MV pipeline

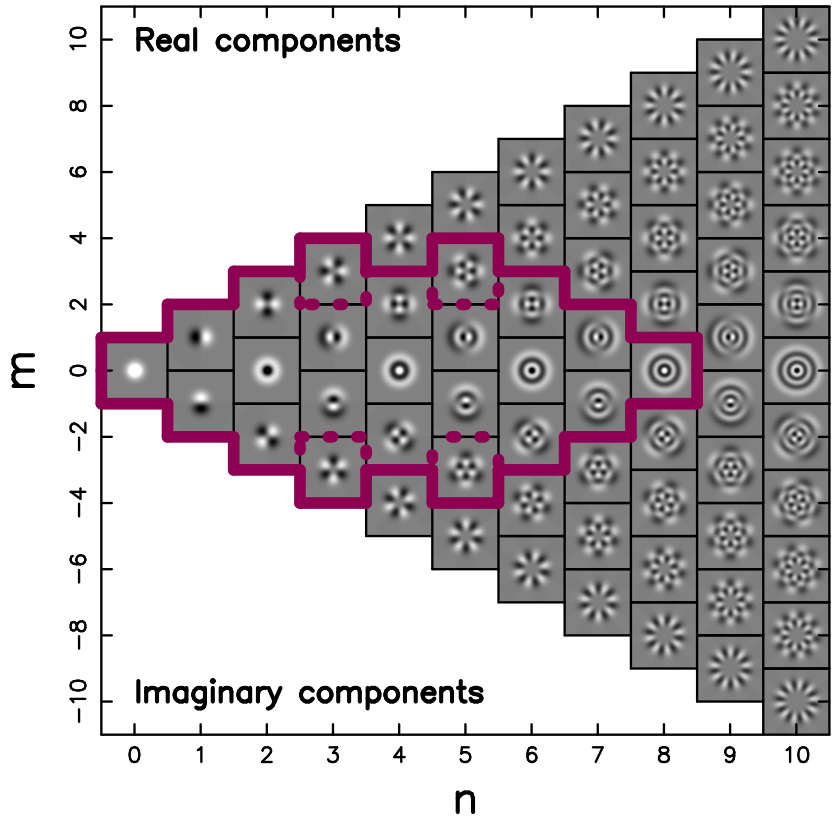

Figure 2.1 Polar Shapelets basis functions up to a maximum Shapelets order of $n_{\rm max} = 10$. For $m \geq 0$, the real components of the basis functions are shown while for $m < 0$ the imaginary components are shown. The solid purple (thick) lines mark the coefficients used by the MV pipeline to estimate the shear and flexions for an analysis with $n_{\rm max} = 10$. The dashed purple (thick) lines mark the coefficients not used by the KK06 implementation for the same $n_{\rm max}$.

The software we introduce and test in this Chapter, the *MV pipeline*, is based on an earlier Shapelets implementation described in Kuijken (2006) (hereafter KK06), which we will refer to as the *KK pipeline*. The KK pipeline is a robust piece of shear estimation software which has been thoroughly tested on simulation suits such as the two Shear TEsting Programmes (STEP1 and STEP2) (Heymans et al., 2006a; Massey et al., 2007a). The MV pipeline keeps the core

Shapelet decompositions of KK, but extends the analysis package to enable flexion measurement. The basic procedure for doing this is to

i) create a circular galaxy model
ii) apply shear and flexion to the model, and convolve with the measured PSF
iii) decompose the true PSF convolved source image into Shapelets
iv) fit the model to the observed image.

In theory a galaxy image could be perfectly described by an infinite series of Shapelets, but in practice we have to truncate this expansion. We choose to truncate at order $n_{\max} = a + b$ (see Equation 2.10). In general we also keep the choice of $n_{\max}$ constant for all galaxies in an analysis, rather than allowing for it to vary according to some criteria such as size or brightness. This ensures that we do not introduce artificial S/N-dependent biases. The trade-off is some noise at higher-order coefficients for smaller or fainter sources but these coefficients will remain unbiased.

Steps i) and ii) above can be summarised as follows to first order in ellipticity s and flexions f and g:

$$\mathbf{P} \cdot \left[1 + \sum_{i=1,2} \left(t_i \hat{T}^i + s_i \hat{S}^i + f_i \hat{F}^i + g_i \hat{G}^i \right) \right] \sum_{\text{even}}^{N_c} c_n C^n \tag{2.23}$$

where $\mathbf{P}$ is the PSF matrix and $\hat{T}^i$, $\hat{S}^i$, $\hat{F}^i$ and $\hat{G}^i$ are the translation, shear, F flexion and G flexion operators respectively, as specified in Equations 2.16–2.21. t_i, s_i, f_i and g_i are the corresponding coefficients which are determined through step iv) above. The translation operators are included in the fit to allow for some shifting to ensure that the fit is not spoilt by an inaccurate centroid. The last term is the circular model in step i) which in this case is expressed as a sum of circular Shapelets C^n with coefficients c_n. n is even (see the $m = 0$ Shapelets in Figure 2.1) and the expansion is truncated at $N_c = n_{\max} - 2$ to safeguard against PSF structure at higher orders affecting the highest order Shapelets used.

Once steps i), ii) and iii) have been carried out, the model galaxy and the cartesian Shapelets representation of the true source image are both converted into polar coordinates in preparation for the fit, as described in Refregier (2003). For cartesian Shapelets of order $n = a + b$, the corresponding polar Shapelets will have order n with angular order $m \leq n$ and $n + m$ even. This conversion is done in order to avoid truncation effects due to the mixing of orders. F flexion, shear and G flexion operators acting on a polar Shapelet of order (n, m) generate terms at order $(n \pm 1, m \pm 1)$, $(n \pm 2, m \pm 2)$ and $(n \pm 3, m \pm 3)$ respectively (see e.g. Massey et al., 2007b, Figure 2, for an illustration of the mixing of Shapelet coefficients). We therefore truncate the polar Shapelets expansion in the diamond shape shown in Figure 2.1, i.e. we only include terms up to order $(N_c, 0)$, $(N_c - 1, \pm 1)$, $(N_c - 2, \pm 2)$ and $(N_c - 3, \pm 3)$ in the fit. This minimises the impact of order mixing. As illustrated in Figure 2.1, the choice of which Shapelets to include in the fit differs slightly between the MV and the KK pipelines. The extra Shapelets included in the MV pipeline are necessitated by the fact that the spin-3 information (i.e. G flexion) is encoded in the $m \pm 3$ components.

Finally in step iv), the model object is fit to the observed source using least-squares. This gives us an estimate for all the relevant quantities simultaneously: the ellipticity (s_1, s_2), the F flexion (f_1, f_2), and the G flexion (g_1, g_2). This technique is fast and adding the four flexion parameters does not significantly increase the computation time compared to fitting for ellipticity alone. The errors on the estimates originate from the errors on the Shapelet coefficients derived from the photon noise. The χ^2 is differentiated at the best-fit in order to obtain covariances between the fit parameters. For further discussion on errors see KK06.

2.3 Monochromatic tests

As part of the development of the KK pipeline, several aspects relevant to the MV pipeline were thoroughly tested. We will therefore not delve further into tests for details which are common between the two, such as the optimal choice of scale radius β and the effect of noise. The distortion measurement routines differ, however, and so we will in this Section thoroughly assess the shear and flexion recovery performance of the MV pipeline. To this end we will use a series of simulations which will be limited to one colour in this Section with the added complication of colour gradients across galaxies and PSFs in the next.

2.3.1 GREAT08

The Gravitational Lensing Accuracy Testing 2008 (GREAT08) challenge (Bridle et al., 2009, 2010) was a competition continuing a tradition of challenges designed to test the accuracy of current state-of-the-art shear measurement software available to the weak lensing community (e.g. STEP1 and STEP2; Heymans et al., 2006a; Massey et al., 2007a). Both the MV pipeline and the KK pipeline were entered in the GREAT08 competition, allowing us to not only test the performance of the MV pipeline under different observing conditions, but also to compare and contrast its shear estimation capabilities to those of its predecessor.

Simulations

The GREAT08 challenge provided simulations designed for testing the fundamentals of shape measurement. Since part of the philosophy of the project was to entice the participation of other communities, such as computer programmers, the simulations were kept fairly simplistic and focused on the core problem of taking a noisy distorted galaxy image and measuring how much it has been sheared by. To avoid any deblending issues, the galaxies were created in individual postage stamps which were then placed on a grid to create an image of 4000×4000 pixels and 10 000 galaxies. Each galaxy postage stamp was created by i) simulating an elliptical and sheared galaxy; ii) convolving it with a PSF; iii) binning the light to create a pixellised image; iv) applying a noise model. During the course of the challenge there were four sets of simulations released to participants; two sets with known shears (low and real noise) and two blind sets (low and real noise). The main challenge consisted of the blind real noise set which consisted of 2 700 composite images as described above.

Table 2.1 Different branches of the GREAT08 RealNoise_Blind simulations. Four parameters were varied between branches according to this table, with further explanations in the text.

	Fiducial	Variation 1	Variation 2
S/N	20	10	40
R_g/R_p	1.40	1.22	1.60
PSF type	Fid	Fid rotated	Fid $e \times 2$
Galaxy type	b+d	b or d	b+d offcentre

Observing conditions were varied between images, one at a time, with the 9 different branches shown in Table 2.1. The fiducial branch had galaxies with S/N = 20 and a ratio between the radius of the PSF convolved galaxy and that of the PSF of $R_g/R_p = 1.40$. These numbers were varied to create four additional branches. The PSF used for all images was a truncated Moffat profile which was mildly elliptical in the horizontal direction for the fiducial branch. The PSF was rotated 45° or its ellipticity was doubled to create two additional branches. The final variable to be altered was the galaxy type. In the fiducial case galaxies were represented by the sum of two Sérsic profiles (Sérsic, 1968) corresponding to the bulge and disk components. For one branch, the galaxies consisted of only one Sérsic profile corresponding to either a bulge or a disk, and in another the centroids of the bulge and disk did not coincide. For more details on the different branches see the GREAT08 results paper (Bridle et al., 2010).

Both the applied shear and the PSF was kept constant across each image, although they were varied between images. The true shear values were concealed from the participants, and so was the information pertaining to which image was part of which of the 9 branches, but the PSF was provided as a star image. Participants were thus told which of the three PSFs had been applied to which image. The true applied shear values were perturbations around 5 root values, both positive and negative, with $|\gamma_{1,2}^{\rm root}| \leq 0.037$. The GREAT08 team utilised the paired rotation technique introduced in STEP2 whereby each simulated galaxy has a twin galaxy which has been rotated by 90° before shearing. This method minimises shape noise since the ellipticity estimates of each pair should cancel in the absence of applied shear and PSF. The large number of simulated galaxy images in combination with this shape noise minimisation technique allowed for high precision assessment of current shape measurement methods in preparation for future surveys.

Results

For the submitted results, we used the MV pipeline and a maximum Shapelets order of $n_{\rm max} = 8$. To average over all the galaxies in an image we used a technique known as convex hull peeling (CHP). CHP works essentially like a 2D median and is a way of eliminating outliers from a sample in a 2D parameter space (e.g. in the (γ_1, γ_2) plane). This is done by removing a so-called convex hull, i.e. the minimal convex set of data points containing all other points. By peeling away a number of convex hulls and averaging over the remaining points, a mean unaffected by extreme results may be produced (see Figure 2.2).

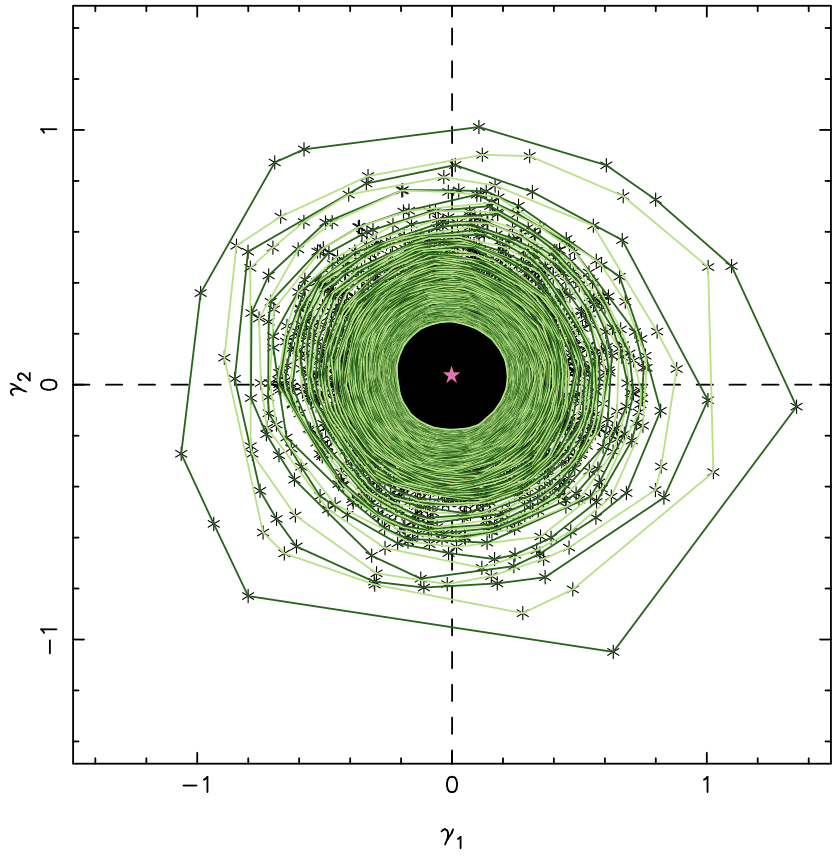

Figure 2.2 Illustration of the convex hull peeling procedure applied to the shears measured on all galaxies in a single GREAT08 image. Each asterisk represents a shear measurement, and the lines connecting data points show the points in the convex hulls being removed before averaging. The final average, after removing 50% of the data points this way, is marked by a red star.

The choice of how many points are removed before averaging may be varied according to their distribution. For GREAT08 we chose to remove 50% of the measurements before averaging.

The GREAT08 team compare the different submissions using a quality factor, or Q-value, in an attempt to consolidate the m (multiplicative bias) and c (additive bias) parameters of STEP into a single quantity. In this case, the Q-value is defined as

$$Q = \frac{k_Q \sigma^2}{\langle (\langle \gamma_{ij}^m - \gamma_{ij}^t \rangle_{j \in k})^2 \rangle_{ikl}} \tag{2.24}$$

where $\sigma^2 = \sigma^2_{\rm stat} + \sigma^2_{\rm syst}$ is a combination of the statistical spread in the simulations and the expected systematic errors. The superscripts m and t denote measured and true values respectively and γ_{ij} is the shear component i for simulation image j. The differences between the measured and true shears are averaged over root shear sets k and simulation branches l. The whole expression is normalised by k_Q such that a method with a purely statistical spread in

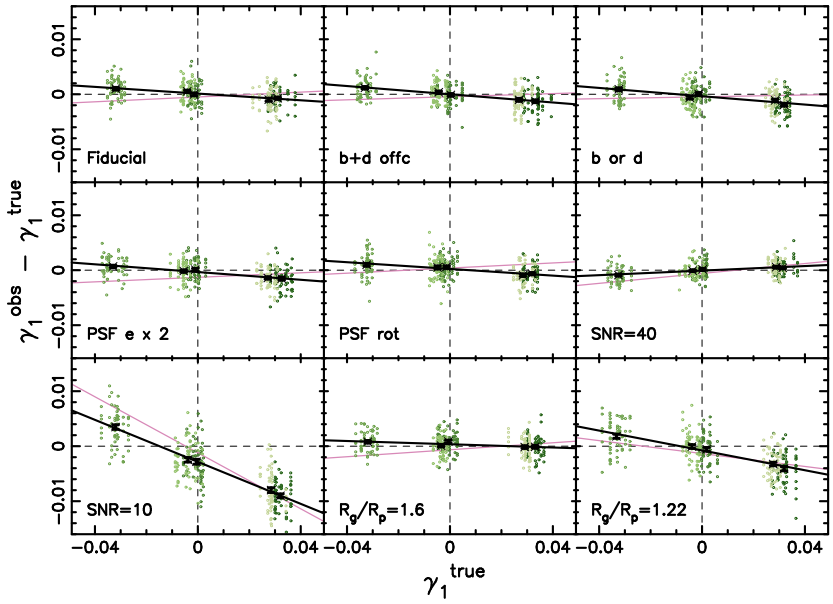

Figure 2.3 Submitted MV γ_1 results for GREAT08. Each circle represents the average γ_1 in a single image containing 10 000 galaxies, and the crosses with error bars show the resulting average for each root shear value. The fitted black line would coincide with the zero-line if there were no biases in the measurements. Also shown as a thinner pink line are the results submitted using the KK pipeline. Each panel represents a different simulation branch as specified in the bottom left corner of each panel (see also Table 2.1). The MV method does well in all cases apart from low signal-to-noise (bottom left panel) and small galaxies (bottom right panel).

the measured shears will have a Q-value of k_Q which is the level desirable for future surveys. In the case of GREAT08, $k_Q = 1000$ and $\sigma^2 = 10^{-7}$, giving a Q-value nominator of 10^{-4}. Established shape measurements at the time of the challenge, such as those based on the KSB method (Kaiser, Squires, & Broadhurst, 1995), generally achieve $10 \lesssim Q \lesssim 100$. For future surveys with greater requirements on accuracy, we would ideally use methods with $Q \to 1000$.

Both the MV and KK pipelines performed well for current surveys, reaching an overall $Q \sim 25$ in the RealNoise_Blind simulations. Due to the definition of Q however, a method is severely penalised if it presents issues in even one of the nine branches. This ensures that a method with a stable high Q across all branches wins the challenge. It is never the less instructive to look at the different branches separately to assess the impact of different observing conditions on the performance of a particular method. In Figures 2.3 and 2.4 we show the residual shear versus true shear for each branch for the submitted MV γ_1 and γ_2 results respectively. From this it is clear that the MV pipeline does very well in 7 of the 9 branches ($100 \lesssim Q_{\rm MV} \lesssim 500$). For a perfect measurement, the black solid line which has been fitted to the data would coincide with the zero-line and any deviation is parameterised via the STEP m and c parameters, defined as follows:

$$\langle \gamma_i^m \rangle - \gamma_i^t = m_i \gamma_i^t + c_i \tag{2.25}$$

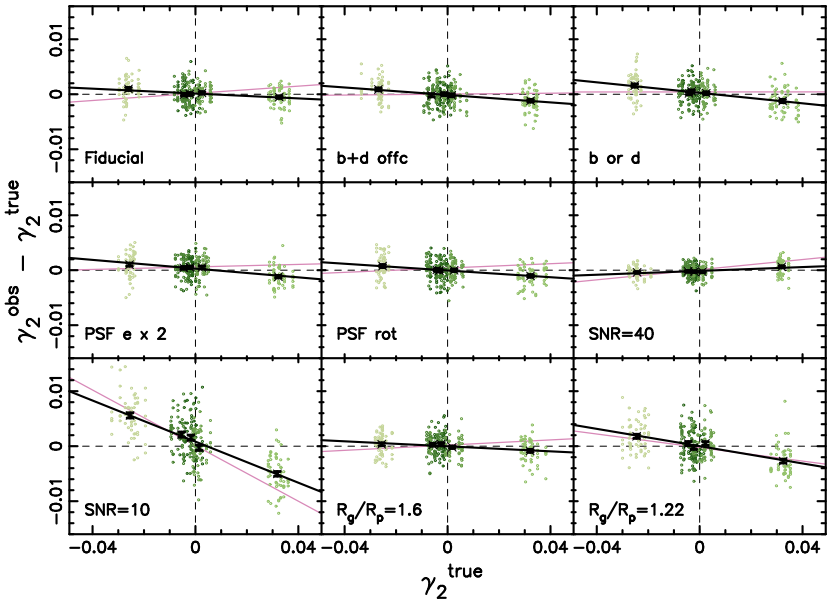

Figure 2.4 Submitted MV γ_2 results for GREAT08. Each circle represents the average γ_2 in a single image containing 10 000 galaxies, and the crosses with error bars show the resulting average for each root shear value. The fitted line would coincide with the zero-line if there were no biases in the measurements. Also shown as a thinner pink line are the results submitted using the KK pipeline. Each panel represents a different simulation branch as specified in the bottom left corner of each panel (see also Table 2.1). The MV method does well in all cases apart from low signal-to-noise (bottom left panel) and small galaxies (bottom right panel).

where $i = 1, 2$ represents the shear component. A negative multiplicative bias m_i thus indicates that the distortion is generally underestimated. A systematic offset c_i may be caused by e.g. insufficient PSF correction, and the Q-values and m and c biases for each of the 9 branches for the MV pipeline may be found in Table 2.2. Also shown for comparison in each panel of Figures 2.3 and 2.4 are the results of the KK pipeline, and the differences in accuracy between the two is small in most cases. A minor distinction is that while the MV pipeline seems to underestimate the shear in nearly all panels, the KK pipeline predominantly overestimates it. For the faint and barely resolved sources, however, both pipelines show similar trends.

Although the MV pipeline performs very well in most cases, the results for faint galaxies (bottom left panels in Figures 2.3 and 2.4) and, to a lesser extent, barely resolved galaxies (bottom right panels) cause the overall Q-value to not reach values adequate for future surveys. The KK pipeline also severely underestimates the shear, and even more so than the MV pipeline in the case of faint galaxies. The strong bias at S/N = 10 is however not consistent with the results found in the STEP challenges (for the KK pipeline; see Heymans et al., 2006a; Massey et al., 2007a) or in our own simulations (for the MV pipeline; see Section 2.3.2). One of the reasons for this discrepancy may be due to the definition of S/N. In GREAT08, the flux of a simulated object is set such that

Table 2.2 MV results for the different branches of the RealNoise_Blind simulations. The Q, m and c parameters are defined in the text (Equations 2.24 and 2.25); the larger the Q-value and the smaller the m and c, the better the recovery of the input shear.

	Q	m_1 ($\times 10^{-2}$)	m_2 ($\times 10^{-2}$)	c_1 ($\times 10^{-4}$)	c_2 ($\times 10^{-4}$)
Fiducial	241	-3.05 ± 0.43	-2.18 ± 0.56	0.24 ± 1.02	1.29 ± 0.99
b+d offset	152	-3.64 ± 0.44	-3.76 ± 0.56	0.83 ± 1.05	-0.37 ± 1.13
b or d	88.9	-4.42 ± 0.48	-4.90 ± 0.67	-2.96 ± 1.15	2.69 ± 1.21
PSF $e \times 2$	140	-3.37 ± 0.44	-3.59 ± 0.56	-3.36 ± 1.03	2.08 ± 1.03
PSF rot	173	-3.09 ± 0.45	-3.88 ± 0.60	2.05 ± 1.10	-1.28 ± 1.08
S/N = 40	471	2.06 ± 0.32	2.20 ± 0.39	-1.14 ± 0.76	-0.65 ± 0.70
S/N = 10	4.81	-18.72 ± 0.70	-20.79 ± 1.03	-17.42 ± 1.74	5.75 ± 1.81
$R_g/R_p = 1.6$	395	-1.60 ± 0.46	-2.39 ± 0.59	3.09 ± 1.11	-0.68 ± 1.03
$R_g/R_p = 1.22$	23.9	-8.76 ± 0.62	-8.41 ± 0.82	-8.05 ± 1.46	0.41 ± 1.57

the number quoted as the signal-to-noise ratio is equal to the total flux divided by the uncertainty in the flux obtained if the true shape, but not normalization, of the object is known. We find that this does not correspond to the S/N we detect as observers, defined as the total observed flux divided by the uncertainty in the flux measurement (as determined by e.g. SExtractor). With this definition we find that GREAT08 simulations with $\mathrm{S/N}_{\mathrm{GREAT08}} = 10, 20, 40$ actually correspond to an observed $\mathrm{S/N}_{\mathrm{obs}} = 6, 12, 23$ respectively, and our results are then more in agreement with previous tests. In real applications we do generally exclude galaxies with $\mathrm{S/N}_{\mathrm{obs}} < 10$ precisely because we know that the bias increases steeply below this level. It should be noted, however, that most galaxies in a weak lensing survey are small and faint, so a shape measurement which is unbiased down to low S/N is vital for future surveys, and it is clear that more work is required in this area. In general though the MV pipeline did exceptionally well under "good" observing conditions, e.g. for the high S/N branch or for well resolved galaxies. Our own simulations described in the next section will further test the dependence of the MV performance on different observing conditions.

2.3.2 FLASHES

In GREAT08, no flexion field has been applied so we are not able to test that aspect of the MV pipeline using those simulations. Because the addition of flexion measurements is the main development since the KK pipeline and all the tests performed on it, it is essential that flexion recovery is tested as well. With no public flexion simulations available, we create our own Flexion and Shear Simulations (FLASHES) using software closely related to the Monte-Carlo selection software used to create the GREAT08 simulations. FLASHES are created with the intent of testing the MV pipeline in preparation for an analysis of the space-based Cosmic Evolution Survey (COSMOS; Scoville et al., 2007), and so several observing conditions are optimised for that survey.

Table 2.3 The different branches of FLASHES. Four parameters are varied between the branches according to this table.

	Intrinsic shape	Galaxy profile	S/N	PSF
Fiducial	Round	Gaussian	100	Round
Shape branch	Elliptical	Gaussian	100	Round
Profile branch 1	Round	Exponential	100	Round
Profile branch 2	Round	de Vaucouleur	100	Round
S/N branch 1	Round	Gaussian	8	Round
S/N branch 2	Round	Gaussian	20	Round
S/N branch 3	Round	Gaussian	40	Round
PSF branch	Round	Gaussian	100	Elliptical

Simulations

The simulation creation technique is not the only similarity between GREAT08 and FLASHES. We create images containing 10 000 galaxies on a grid, with a pair-wise match of intrinsic ellipticities in the case of elliptical galaxies. And just as in GREAT08, each galaxy is created by i) simulating a lensing distorted (elliptical) galaxy; ii) convolving it with a PSF; iii) binning the light to create a pixellised image; iv) applying a noise model. However, since this is not a challenge but an investigation into the behaviour of our pipeline, we choose different observational conditions to GREAT08 and generally the S/N is kept high. An overview of the 8 branches of FLASHES is shown in Table 2.3. All galaxies are approximated as single-component Sérsic intensity profiles (rather than the bulge-plus-disk description of GREAT08), with the fiducial profile being a circular Gaussian, i.e. an intensity profile with Sérsic index $n = 0.5$. For one branch this index is set to $n = 1$ instead, corresponding to an exponential profile, and in another the index is $n = 4$, creating a de Vaucouleur profile. For the branch with intrinsic ellipticities we pick random ellipticities from the distribution in COSMOS and to minimise shape noise we use the paired rotation technique as described in the previous section. We do not, however, include any intrinsic flexion in these simulations. While we allow the lensing distortion to vary between images, it is kept constant for all galaxies across a single image. The strength of the shear and flexion fields are picked randomly but we ensure that the value never exceeds $|\gamma_{1,2}| \leq 0.05$, $|\mathcal{F}_{1,2}| \leq 0.008$ pixel^{-1} and $|\mathcal{G}_{1,2}| \leq 0.02$ pixel^{-1}.

Once a lensing distorted galaxy model has been created we convolve it with a PSF which is described by a Moffat profile with an index $m = 9$, making it nearly Gaussian. This PSF is circular in general, except for one branch where it is elliptical in the horizontal direction with $e_{1,\mathrm{PSF}} = 0.02$. As these simulations are intended to mimic COSMOS data, the size of the PSF is fairly small with a full width at half maximum (FWHM) of 2.1 pixels, resulting in a PSF convolved galaxy size of 5.8 pixels. Finally we use the definition of $\mathrm{S/N}_{\mathrm{obs}}$ from the previous section to define the four S/N branches. Most of the tests are carried out under near-perfect noise conditions to highlight any noise-independent biases, but the lower S/N branches have the function of showing the impact of noise on shape measurement accuracy. The lowest S/N = 8 branch shows the bias below the S/N = 10 cut we generally apply when using real data.

Results

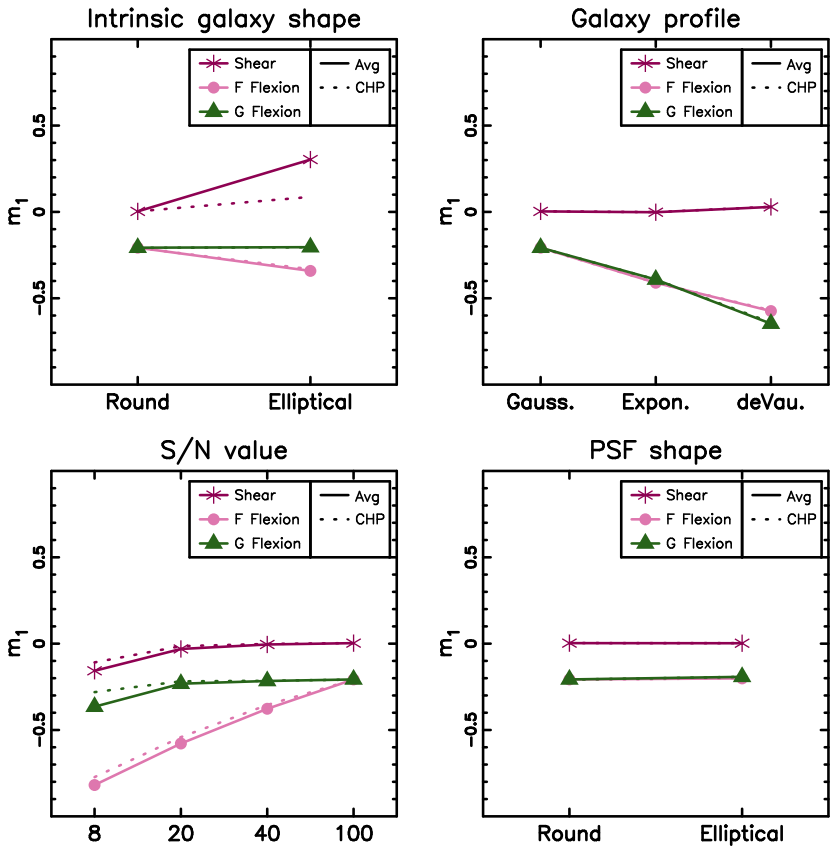

Figure 2.5 The multiplicative bias m on the first component for each of shear, F flexion and G flexion. The purple stars, pink circles and green triangles represent shear, F flexion and G flexion respectively. The symbols and solid lines show the weighted averages while the dashed lines show the CHP average. This is from running the MV pipeline on FLASHES with $n_{\max} = 10$.

The version of the MV pipeline tested on FLASHES is the same as that tested in GREAT08, with one minor difference; since the galaxies are in general better resolved we use a maximum Shapelets order of $n_{\max} = 10$. The galaxy shapes in each image are averaged using two separate methods: CHP as in GREAT08, and a weighted average with weights inversely proportional to the measurement errors. To quantify the performance we use the m and c parameters from STEP only rather than calculating a Q-value, or equivalent for flexion. The results for m_1 and c_1 are shown in Figures 2.5 and 2.6 respectively, and the fitted biases are detailed in Table 2.4. The biases and their trends are all very similar for the second component and so we choose not to show them here. It is clear from this that though the shear can be recovered with an accuracy of a few per cent in general, the flexions are likely to be underestimated. This is particularly true for higher Sérsic indices and noisier data. The dependence on galaxy brightness profile is most likely an effect of the fact that Shapelets consists of Gauss-

Table 2.4 First component multiplicative and additive biases in the MV pipeline based on FLASHES. The top, middle and bottom tables show the shear, F flexion and G flexion results respectively. Both results using a weighted average (superscript avg) and convex hull peeling (superscript CHP) are displayed. For details on the branches, see Table 2.3.

	Shear			
	$m_{1,\gamma}^{\mathrm{avg}}$ $(\times 10^{-2})$	$c_{1,\gamma}^{\mathrm{avg}}$ $(\times 10^{-4})$	$m_{1,\gamma}^{\mathrm{CHP}}$ $(\times 10^{-2})$	$c_{1,\gamma}^{\mathrm{CHP}}$ $(\times 10^{-4})$
Fiducial	0.29 ± 0.10	1.75 ± 0.11	0.33 ± 0.10	1.80 ± 0.11
Shape branch	30.31 ± 0.10	-2.52 ± 5.11	8.68 ± 0.13	-0.96 ± 5.11
Profile branch 1	-0.16 ± 0.06	-6.85 ± 0.12	-0.10 ± 0.06	-6.75 ± 0.12
Profile branch 2	2.92 ± 0.30	-3.39 ± 1.70	2.95 ± 0.32	-2.68 ± 1.70
S/N branch 1	-15.73 ± 0.15	1.02 ± 1.86	-10.86 ± 0.10	6.09 ± 1.86
S/N branch 2	-3.05 ± 0.09	2.15 ± 0.59	-1.44 ± 0.10	2.81 ± 0.59
S/N branch 3	-0.51 ± 0.09	4.87 ± 0.32	-0.15 ± 0.09	5.01 ± 0.32
PSF branch	0.25 ± 0.07	3.36 ± 0.11	0.31 ± 0.07	3.38 ± 0.11

	F flexion			
	$m_{1,\mathcal{F}}^{\mathrm{avg}}$ $(\times 10^{-2})$	$c_{1,\mathcal{F}}^{\mathrm{avg}}$ $(\times 10^{-4})$	$m_{1,\mathcal{F}}^{\mathrm{CHP}}$ $(\times 10^{-2})$	$c_{1,\mathcal{F}}^{\mathrm{CHP}}$ $(\times 10^{-4})$
Fiducial	-20.70 ± 0.05	4.83 ± 0.00	-20.84 ± 0.05	4.85 ± 0.00
Shape branch	-34.15 ± 0.03	1.12 ± 0.00	-33.16 ± 0.03	1.18 ± 0.00
Profile branch 1	-41.00 ± 0.01	-2.24 ± 0.00	-41.06 ± 0.01	-2.24 ± 0.00
Profile branch 2	-57.41 ± 0.03	-2.99 ± 0.00	-57.00 ± 0.04	-2.95 ± 0.00
S/N branch 1	-81.87 ± 0.02	1.41 ± 0.03	-77.27 ± 0.03	2.14 ± 0.03
S/N branch 2	-57.83 ± 0.02	2.84 ± 0.01	-54.16 ± 0.02	3.22 ± 0.01
S/N branch 3	-37.69 ± 0.04	3.16 ± 0.00	-35.51 ± 0.04	3.29 ± 0.00
PSF branch	-20.13 ± 0.03	4.52 ± 0.00	-20.03 ± 0.03	4.51 ± 0.00

	G flexion			
	$m_{1,\mathcal{G}}^{\mathrm{avg}}$ $(\times 10^{-2})$	$c_{1,\mathcal{G}}^{\mathrm{avg}}$ $(\times 10^{-4})$	$m_{1,\mathcal{G}}^{\mathrm{CHP}}$ $(\times 10^{-2})$	$c_{1,\mathcal{G}}^{\mathrm{CHP}}$ $(\times 10^{-4})$
Fiducial	-20.73 ± 0.04	-7.48 ± 0.00	-20.81 ± 0.04	-7.41 ± 0.00
Shape branch	-20.40 ± 0.04	-2.18 ± 0.00	-20.47 ± 0.04	-2.20 ± 0.00
Profile branch 1	-39.17 ± 0.03	0.09 ± 0.00	-39.16 ± 0.03	0.06 ± 0.00
Profile branch 2	-64.68 ± 0.15	3.78 ± 0.01	-64.03 ± 0.17	4.29 ± 0.01
S/N branch 1	-36.52 ± 0.08	-7.77 ± 0.24	-28.07 ± 0.11	-8.71 ± 0.24
S/N branch 2	-23.22 ± 0.03	-6.90 ± 0.03	-21.80 ± 0.03	-7.43 ± 0.03
S/N branch 3	-21.62 ± 0.04	-7.88 ± 0.01	-21.51 ± 0.04	-7.88 ± 0.01
PSF branch	-19.21 ± 0.03	-8.37 ± 0.00	-19.22 ± 0.04	-8.47 ± 0.00

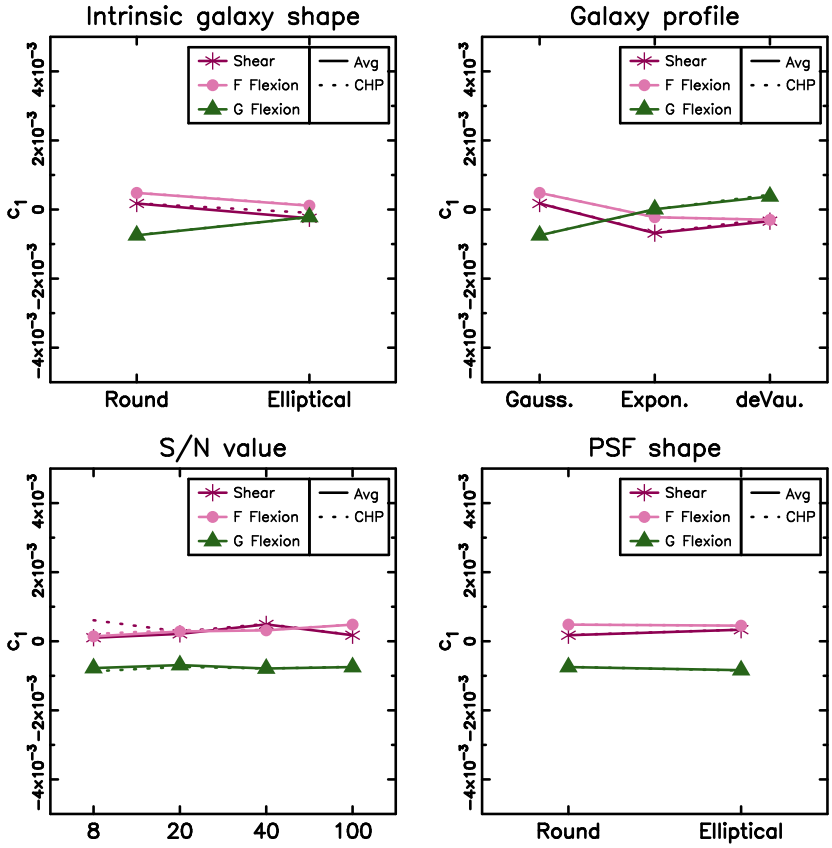

Figure 2.6 The additive bias c on the first component for each of shear, F flexion and G flexion. The purple stars, pink circles and green triangles represent shear, F flexion and G flexion respectively. The symbols and solid lines show the weighted averages while the dashed lines show the CHP average. This is from running the MV pipeline on FLASHES with $n_{\max} = 10$.

Hermite basis functions so it will be optimised for profiles similar to Gaussian profiles. As the Sérsic index increases, the central peak becomes sharper and any skewness (e.g. F flexion) may get more affected by the diluting effect of the PSF, effectively drowning out the F flexion signal. Additionally the wings of the profile reach further which means that very high order Shapelets are required to model them. However, a maximum Shapelets order of $n_{\max} = 10$ necessitates the fitting of 66 free parameters during the galaxy image decomposition stage, and a typical galaxy in these simulations only covers an area of ~ 80 pixels. Including much higher orders than already done will therefore entail fitting noise, and so we keep our maximum Shapelets order at 10. The consequence is that some information in the outer wings is not modelled, and this in turn leads to an underestimation of the flexions for higher Sérsic indices. The G flexion also displays a non-negligible systematic offset c for galaxies with fiducial Gaussian profiles, which may be a sign that this particular combination of galaxy brightness and PSF profiles causes a spurious G flexion signal.

The F flexion is more sensitive to noise than shear or G flexion, as is evident from the lower left panel of Figure 2.5. While shear and G flexion show more bias for the lowest S/N value of 8, a dataset which would be deemed too noisy in an analysis of real data, than for other values, the F flexion shows a trend of greater underestimation even for reasonably high S/N galaxies. A S/N cut is therefore essential, but for F flexion a more sophisticated treatment is necessary to calibrate the measurements. FLASHES have been designed to test the performance of the MV pipeline under COSMOS-like observing conditions. We use our findings to correct for any effects due to noise biases in our analysis of the COSMOS survey (see Chapter 3). It should be noted, however, that as of yet too little is known about potential biases under different observing conditions, so calibrating shape measurements in any other survey based on FLASHES alone is not recommended.

2.4 Non-monochromatic tests

As made clear, the PSF of a telescope will, if left uncorrected for, bias galaxy shape measurements. For a broad-band filter, such as the one included in the design of the future space-based mission Euclid, additional complications arise from the fact that the PSF usually depends on wavelength. Hence, since the colour generally varies across a galaxy, which is likely to have a redder central bulge and a bluer disk, the PSF will as well. We therefore have to determine how galaxy colour gradients affect our ability to recover the true lensing distortions, represented by shear in this Section.

2.4.1 Analytical prediction

To assess the possibility to correct for the effect of a colour-dependent PSF, we describe the observed intensity, $I^{\rm obs}(\boldsymbol{\theta})$, of a galaxy image observed in a filter of finite bandwidth as an integral over wavelength:

$$I^{\rm obs}(\boldsymbol{\theta}) = \int d\lambda\, I^{\rm obs}(\boldsymbol{\theta},\lambda) \tag{2.26}$$

$$= \int d\lambda\, I^{0}(\boldsymbol{\theta},\lambda) \otimes T(\boldsymbol{\theta},\lambda) \tag{2.27}$$

where we have made explicit that the observed intensity is the pre-seeing intensity $I^0(\boldsymbol{\theta},\lambda)$ viewed through an imaging system with a PSF $T(\boldsymbol{\theta},\lambda)$. For a broad filter, the observed centroid is

$$\bar{\theta}_i \equiv \frac{1}{F_{\rm tot}} \int d\lambda \int d\boldsymbol{\theta}\; \theta_i I^{\rm obs}(\boldsymbol{\theta},\lambda) \tag{2.28}$$

$$= \frac{1}{F_{\rm tot}} \int d\lambda \int d\boldsymbol{\theta} \int d\boldsymbol{\varphi}\; \theta_i I^{0}(\boldsymbol{\varphi},\lambda) T(\boldsymbol{\theta}-\boldsymbol{\varphi},\lambda) \tag{2.29}$$

where $F_{\rm tot}$ is the total flux. By employing a change in variable, $\mathbf{x} = \boldsymbol{\theta} - \boldsymbol{\varphi}$, we can derive the following expression:

$$\bar{\theta}_i = \frac{1}{F_{\rm tot}} \int d\lambda \int d\boldsymbol{\theta} \int d\mathbf{x}\; \left[I^{0}(\boldsymbol{\theta},\lambda)\varphi_i T(\mathbf{x},\lambda) + I^{0}(\boldsymbol{\theta},\lambda) x_i T(\mathbf{x},\lambda)\right] \tag{2.30}$$

$$= \frac{1}{F_{\rm tot}} \int d\lambda\; \left[\theta_i(\lambda) F(\lambda) + F(\lambda) p_i(\lambda) T(\lambda)\right] \tag{2.31}$$

where, for a given wavelength λ, $F(\lambda)$ is the total flux, $\theta_i(\lambda)$ is the centroid, $p_i(\lambda)$ are the first-order moments of the PSF and $T(\lambda) = \int d\boldsymbol{\theta}\ T(\boldsymbol{\theta}, \lambda)$. For a symmetric PSF the term $\int d\mathbf{x}\ I^0(\boldsymbol{\theta}, \lambda) x_i T(\mathbf{x}, \lambda)$ will vanish; for more complicated PSFs (such as imaging affected by coma) the term may be evaluated if the PSF moments are known.

Assuming that the centroids for all wavelengths coincide for each galaxy, we can estimate the pre-seeing centroid using Equation 2.31. We therefore continue our analysis using centred moments. The second-order unweighted moments of the pre-seeing and post-seeing intensities, Q^0_{ij} and $Q^{\rm obs}_{ij}$, and of the PSF, P_{ij}, are defined as

$$
\begin{aligned}
Q^0_{ij} &= \frac{1}{F_{\rm tot}} \int d\lambda \int d\boldsymbol{\theta}\ \theta_i \theta_j I^0(\boldsymbol{\theta}, \lambda) && (2.32)\\
Q^{\rm obs}_{ij} &= \frac{1}{F_{\rm tot}} \int d\lambda \int d\boldsymbol{\theta}\ \theta_i \theta_j I^{\rm obs}(\boldsymbol{\theta}, \lambda) && (2.33)\\
&= \frac{1}{F_{\rm tot}} \int d\lambda \int d\boldsymbol{\theta}\ \theta_i \theta_j \int d\boldsymbol{\varphi}\ I^0(\boldsymbol{\varphi}, \lambda) T(\boldsymbol{\theta} - \boldsymbol{\varphi}, \lambda) && (2.34)\\
P_{ij}(\lambda) &= \frac{1}{T(\lambda)} \int d\boldsymbol{\theta}\ \theta_i \theta_j T(\boldsymbol{\theta}, \lambda) && (2.35)
\end{aligned}
$$

Using the same substitution as above we can rewrite Equation 2.34 as

$$
Q^{\rm obs}_{ij} = \frac{1}{F_{\rm tot}} \int d\lambda \int d\boldsymbol{\varphi}\ I^0(\boldsymbol{\varphi}, \lambda) \int d\mathbf{x}\ T(\mathbf{x}, \lambda)(x_i x_j + \varphi_i \varphi_j + x_i \varphi_j + \varphi_i x_j) \tag{2.36}
$$

The two latter terms can be eliminated since the centroid of the pre-seeing galaxy is assumed to be independent of wavelength. We then have

$$
\begin{aligned}
Q^{\rm obs}_{ij} &= \frac{1}{F_{\rm tot}} \int d\lambda \left[\int d\boldsymbol{\varphi}\ I^0(\boldsymbol{\varphi}, \lambda) \int d\mathbf{x}\ T(\mathbf{x}, \lambda) x_i x_j \right.\\
&\qquad \left. + \int d\boldsymbol{\varphi}\ I^0(\boldsymbol{\varphi}, \lambda) \varphi_i \varphi_j \int d\mathbf{x}\ T(\mathbf{x}, \lambda) \right] && (2.37)
\end{aligned}
$$

which may be rewritten as before:

$$
Q^{\rm obs}_{ij} = \frac{1}{F_{\rm tot}} \int d\lambda\ \left[F(\lambda) P_{ij}(\lambda) T(\lambda) + Q^0_{ij}(\lambda) F(\lambda) T(\lambda) \right] \tag{2.38}
$$

i.e.

$$
Q^0_{ij} = Q^{\rm obs}_{ij} - \frac{1}{F_{\rm tot}} \int d\lambda\ T(\lambda) F(\lambda) P_{ij}(\lambda) \tag{2.39}
$$

Equation 2.39 shows that to measure second-order unweighted moments, and thus shear, we only need to know $F(\lambda)$ and $P_{ij}(\lambda)$. Assuming accurate knowledge of $F(\lambda)$, we conclude that for a perfect shape measurement method colour gradient will not cause systematic errors to dominate the error budget. However, using unweighted moments to estimate shear is not possible due to noise. Methods in use today use either weighted moments or a fitting procedure such as Shapelets, and both techniques are equivalent to a weighting scheme.

Now, assuming that we know the effective PSF, a valid assumption according to Cypriano et al. (2010), we may use the wavelength-integrated image $I^{\rm obs}(\boldsymbol{\theta})$ to derive an estimate of the pre-seeing image $I^{\rm est}(\boldsymbol{\theta})$:

$$
I^{\rm obs}(\boldsymbol{\theta}) = I^{\rm est}(\boldsymbol{\theta}) \otimes \int d\lambda\ F(\lambda) T(\boldsymbol{\theta}, \lambda) \tag{2.40}
$$

where as above, $F(\lambda)$ is the flux of the galaxy at a given wavelength and $I^{\rm est}(\boldsymbol{\theta})$ is not necessarily equal to $I^0(\boldsymbol{\theta}, \lambda)$. In the general case there will therefore be a bias since we will not have enough information to reconstruct $I^0(\boldsymbol{\theta}, \lambda)$, even with perfect knowledge of $T(\boldsymbol{\theta}, \lambda)$ and $I^{\rm obs}(\boldsymbol{\theta})$. To quantify this discrepancy we create simulations to mimic galaxies with colour gradients as observed through a broad-band filter.

2.4.2 Simulations

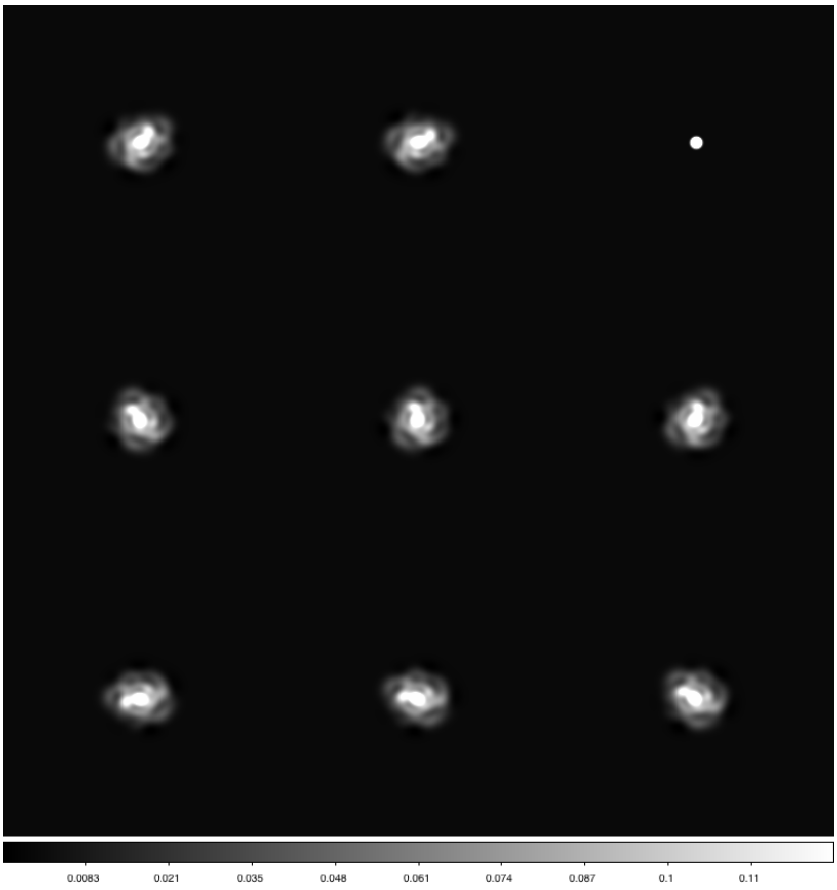

Figure 2.7 Simulated image representative of the simulations created for each galaxy in our sample. There are 8 identical galaxy images rotated in equal steps of 22.5° before a shear has been applied. In the top right corner is a star image representing the PSF.

The simulations we create to assess the impact of colour gradients on shape measurement consist of nearly 20 000 real galaxies taken from the All-Wavelength Extended Groth Strip International Survey (AEGIS; Davis et al., 2007) imaged with the Advanced Camera for Surveys (ACS) onboard the Hubble Space Telescope (HST). Our specific aim here is to evaluate the significance of this bias for Euclid, and the planned diffraction limit of this future telescope is twice the size

of the HST limit. We therefore use only AEGIS galaxies that are well resolved and can thus disregard the small effect of the HST PSF on the images.

Each galaxy has been observed in both the F606W (V-band) and the F814W (I-band) filters, and in general both the size and the flux of a galaxy will be greater in the redder band due in part to morphology and in part to telescope optics. We also have access to photometric redshifts for 11260 objects via the overlap with CFHTLS-Deep3 which gives us the ability to evaluate the bias as a function of redshift. This is in fact an important aspect of our tests because as they evolve, galaxies change morphologies and therefore their colour gradients. Our simulations then consist of a series of images with each one corresponding to a single AEGIS galaxy, as exemplified in Figure 2.7. In order to minimise noise in our simulations we choose not to use the galaxy image directly, but we decompose the observed AEGIS galaxy in each band into Shapelets. This Shapelets representation is then duplicated and rotated to create eight identical galaxy models with different orientations. The differing orientations of the galaxy images allows us to perform a 'ring test' which reduces the noise generated by the intrinsic galaxy morphology. After rotating, the same shear is applied to each galaxy realisation before we convolve them with a PSF and add them to the simulated image using a pixel-scale of 0.05 arcsec. To ensure that their brightness distributions do not overlap we place the galaxies at set positions on the image. A representation of the PSF acting on a point source (a 'star') with the same flux as the galaxy is also inserted in each image of eight galaxy realisations. This allows for the shape measurement software to be run as it normally would be on real survey images.

The shear we apply to our simulated galaxies is relatively large compared to the other simulation sets described in this Chapter, but still well within the weak lensing regime at $\gamma_1 = 0.05$, $\gamma_2 = 0.00$. A subtlety of our approach is that since we use real objects as a basis for our simulations, the original galaxies have already been sheared by foreground structure which results in a slightly different response compared to the true intrinsic galaxy. This effect is small however and will not significantly impact our ability to quantify the bias induced by colour gradients.

To simulate a broad-band Euclid-like PSF, we approximate a diffraction-limited Airy disk using a Gaussian profile with a frequency dependent FWHM. The FWHM is chosen to be $\mathrm{FWHM}_{\mathrm{PSF}}^{F606W} = 0.17$ arcsec for the bluer filter and $\mathrm{FWHM}_{\mathrm{PSF}}^{F814W} = 0.21$ arcsec for the redder one, though we note that the Eculid PSF has extended wings and may therefore effectively be slightly larger. We convolve the galaxy image in the red filter with the red PSF, and similarly for blue. Combining the two as described below results in a total PSF which is the weighted mean of the blue and red PSFs, and which thus has a different response depending on wavelength.

We now have eight sheared and PSF-convolved realisations for each galaxy combined into a single image for each of two narrow filters. To simulate a broad filter similar to the one proposed for Euclid, we stack the two narrow-band images by adding them:

$$I^{\mathrm{obs}}(\boldsymbol{\theta}) = I^{\mathrm{obs},F606W}(\boldsymbol{\theta}) + I^{\mathrm{obs},F814W}(\boldsymbol{\theta}) \quad (2.41)$$

$$= I^{0,F606W}(\boldsymbol{\theta}) \otimes T^{F606W}(\boldsymbol{\theta}) + I^{0,F814W}(\boldsymbol{\theta}) \otimes T^{F814W}(\boldsymbol{\theta}) \quad (2.42)$$

The wavelength-dependent PSF is thus approximated as the sum of two Gaus-

sian profiles of different width:

$$T(\boldsymbol{\theta}, \lambda) \simeq \frac{1}{F_{\rm tot}} \left[F^{F606W} T^{F606W}(\boldsymbol{\theta}) + F^{F814W} T^{F814W}(\boldsymbol{\theta}) \right] \tag{2.43}$$

Since we do not have access to a perfect shape measurement method and thus expect a bias even without colour gradients, we have to quantify the bias associated with the method itself. To this end we create two control images for each set of galaxy realisations. The control images consist of galaxies that have no colour gradient, but that are subjected to the same PSF as the Euclid-like simulations above. Comparing our results on the broad-band simulations to these control images will convey the *additional* bias induced through the assumption of monochromaticity. We thus first convolve the F606W galaxy image with a Gaussian PSF of the same width as the F814W simulation, and vice versa:

$$I^{\rm obs,1}(\boldsymbol{\theta}) = I^{0,F606W}(\boldsymbol{\theta}) \otimes T^{F814W}(\boldsymbol{\theta}) \tag{2.44}$$

$$I^{\rm obs,2}(\boldsymbol{\theta}) = I^{0,F814W}(\boldsymbol{\theta}) \otimes T^{F606W}(\boldsymbol{\theta}) \tag{2.45}$$

To account for the normalisations of the PSFs, we ensure that the control images are created using the appropriate proportions:

$$I^{{\rm ctrl},F606W}(\boldsymbol{\theta}) = I^{{\rm obs},F606W}(\boldsymbol{\theta}) + \frac{F^{F814W}}{F^{F606W}} I^{\rm obs,1}(\boldsymbol{\theta}) \tag{2.46}$$

$$I^{{\rm ctrl},F814W}(\boldsymbol{\theta}) = I^{{\rm obs},F814W}(\boldsymbol{\theta}) + \frac{F^{F606W}}{F^{F814W}} I^{\rm obs,2}(\boldsymbol{\theta}) \tag{2.47}$$

$I^{{\rm ctrl},F606W}$ is thus a galaxy with no colour gradient, but with the intensity distribution observed in F606W and convolved with our approximate Euclid PSF, and similarly for $I^{{\rm ctrl},F814W}$. As mentioned above, the important feature of these two control images is that they both have the same PSF as our broad-band simulation. This is crucial because we have to compare images with identical PSFs in order to avoid introducing another source of bias discrepancy between filters.

We note here that our approach does entail a simplification of the problem since we base our simulations on galaxies observed in two filters which are themselves fairly broad. One of our assumptions is therefore that the colour of a galaxy in one filter is that of the central wavelength, and that the spectral energy distribution (SED) can be approximated through an interpolation between the two filters. Ideally we would use data from several narrower filters, but we do find via analytical tests that this assumption does not impact our knowledge of the bias significantly.

2.4.3 Results

We use the MV pipeline to estimate the shear in both the control images and in the stacked simulated broad-band image. Since we do not have access to a perfect shape measurement method, we want to minimise the bias inherent in the method itself. Our simulations are created with Shapelets, and therefore a Shapelets shear measurement pipeline should be the optimal technique for analysing these images. However, because the PSF consists of two stacked

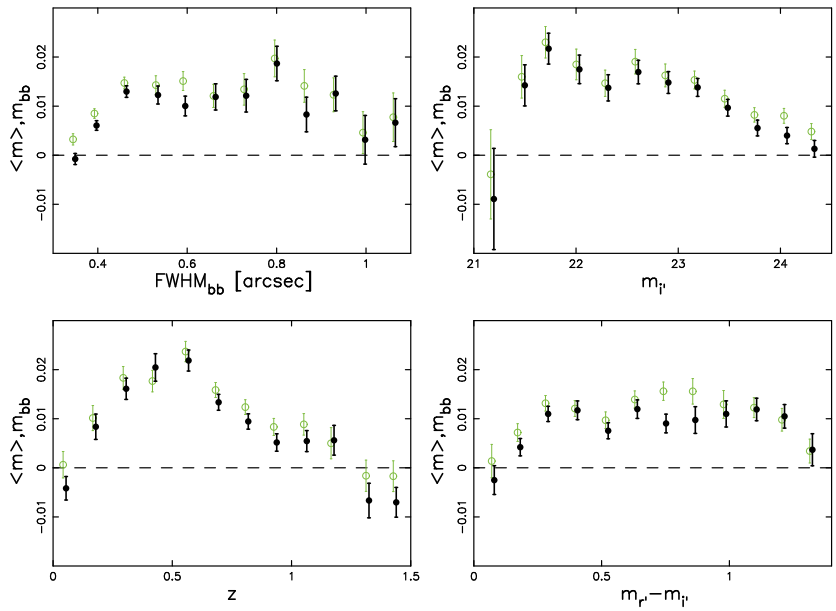

Figure 2.8 Bias measured in the non-monochromatic simulations as a function of different galaxy parameters. Filled black points represent the average multiplicative bias $\langle m \rangle = 0.5(m_{606} + m_{814})$ determined in the narrow-band filters, while open green points represent the bias measured in the Euclid-like stack, m_{bb}. $\mathrm{FWHM_{bb}}$ is the size measured in the stack, and the magnitude and redshift data are obtained via CFHTLS-Deep3.

Gaussian profiles of different widths the resulting simulation is no longer as ideal and thus there will still be a bias present. The control images are therefore vital in determining which bias is due to limitations of the shape measurement method, and which is due to galaxy colour gradients and PSF wavelength dependence.

We determine the multiplicative bias by obtaining the mean shear in each bin, dividing it by the input shear and subtracting 1 such that a perfectly recovered shear would result in $m_{\mathrm{aeg}} = 0$:

$$m_{\mathrm{aeg,bin}} = \frac{\langle \gamma_{1,\mathrm{bin}} \rangle}{\gamma_{1,\mathrm{in}}} - 1 \tag{2.48}$$

where we are only considering the first shear component as the second component has been set to zero at input. The bias we measure in these simulations, as shown in Figure 2.8, is in general positive since the galaxies are very high S/N and the MV pipeline is optimised for images with lower S/N. In the top two panels of Figure 2.8 we display the average bias determined in each filter F606W and F814W, and that measured in the broad-band simulations, as a function of galaxy size and CFHTLS i'-band magnitude. We see that the bias measured initially increases as galaxies become bigger and brighter, and the trend then plateaus. In the lower panel the bias is shown as a function of photometric redshift and colour.

The biases measured in each band only carries information about the partic-

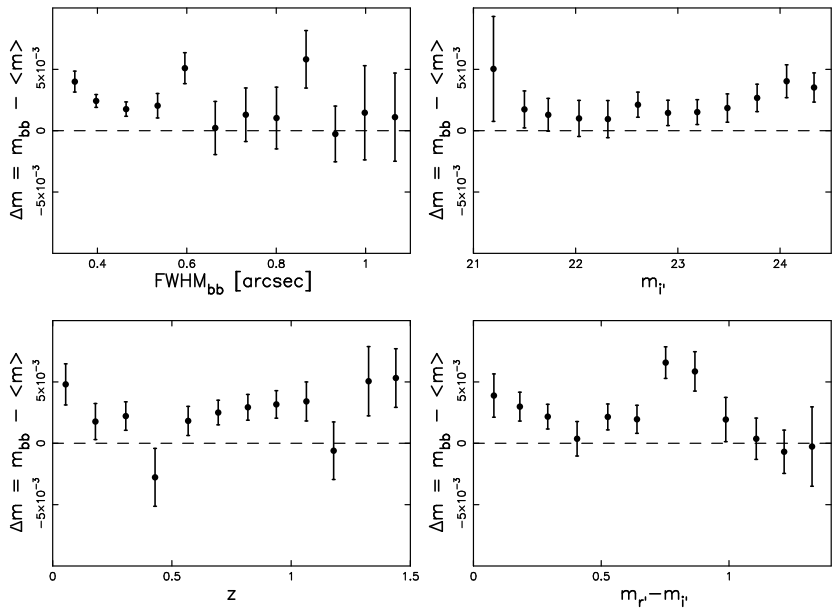

Figure 2.9 Difference between the multiplicative bias measured in the simulated stack, $m_{\rm bb}$, and that measured in the narrow-band filters on average, $\langle m \rangle = 0.5(m_{606} + m_{814})$, as a function of different galaxy parameters. $\mathrm{FWHM_{bb}}$ is the size measured in the stack, and the magnitude and redshift data are obtained via CFHTLS-Deep3.

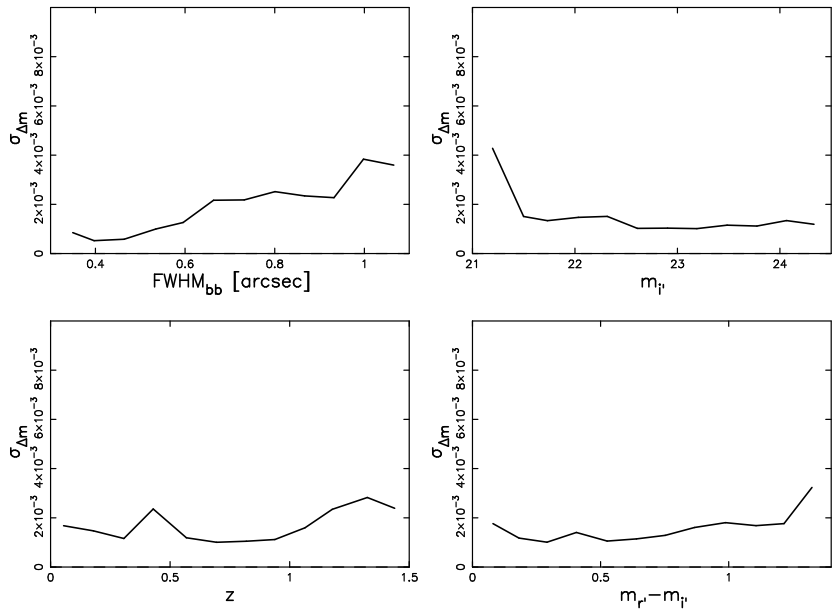

Figure 2.10 Error on the multiplicative bias difference between the simulated stack and the narrow-band images, as a function of galaxy properties.

ular shape measurement method used (the MV pipeline in this case). It is encouraging that the accuracy of the shear measurements is at percent level, but to assess the impact of a wavelength-dependent PSF we have to contrast the accuracy in the broad-band filter with that in each individual narrow-band filter. In Figure 2.9 we therefore show the difference in bias $\Delta m = m_{\rm bb} - 0.5(m_{606} + m_{814})$ as a function of the same parameters as before. Though there is a positive signal, indicating a higher bias in the broad-band filter than in the narrower ones, it is consistently sub-percentage in size so it is much smaller than the bias induced by the shape measurement software. There are some trends in the colour gradient bias, particularly as a function of redshift and average colour. These trends will need to be carefully modelled in order to account for this bias in future surveys. It is still complicated to interpret the results, however, since some of the difference in bias could still be explained by the results in individual bands. If for instance the galaxy is smaller when observed in F606W than when observed in the broad-band filter then the bias in the broad-band filter will be greater simply due to the size-dependence of the bias (see Figure 2.8).

The results we have presented here are an indication of what may be expected in terms of the bias induced by a wavelength-dependent PSF. However, the simulations have been created using two filters only and though these filters are narrower than the one proposed for Euclid, the wavelength resolution may still be too low to properly represent the colour gradient in the observed galaxy. We have also used real galaxies which have been sheared before being observed in AEGIS and this causes a small uncertainty in our bias. With more data observed in several narrow bands we will be able to constrain the bias further, but the results displayed here show that the shape measurement bias induced by assuming monochromaticity despite the use of a broad-band and the loss of colour information that entails, is lower than the bias inherent in the shape measurement method. It is also important to note that due to the noisiness of the shape measurements and due to the limited galaxy sample available, the errors on the additional bias (as shown in Figure 2.10) are a good indication of the true errors. Thus we are able to determine the level of bias, given the constraints described above, accurately. By studying the bias in more detail we will therefore most likely be able to correct for this small effect in surveys such as Euclid.

2.5 Conclusion

We have in this Chapter described and tested a new weak lensing shape measurement software suite with the capability of measuring higher order distortions known as flexion, as well as shear: the MV pipeline. Based on the Shapelets formalism, it is a new incarnation and an extension of the software described in Kuijken (2006) with which it was contrasted in the context of the GREAT08 challenge. The GREAT08 simulations provided an ideal testbed for testing the shear recovery accuracy under different observing conditions. The MV pipeline did very well in this challenge in nearly all regimes with very competitive quality factor values of $Q \sim 100$ and above. The exception was very faint and barely resolved galaxies where the S/N was just too low and this resulted in an overall Q-value of $Q \sim 25$.

To test the MV pipeline for the accuracy of the flexion measurements we

created our own simulations which we named FLASHES. These simulations were generated using software very similar to the one used to produce the GREAT08 simulations, but with the important difference of flexion distortions being added to the lensing potential. FLASHES mimic the survey conditions of the space-based COSMOS survey, and were kept generally low-noise to assess any biases induced by other factors. We confirmed that the input shear could be recovered with high accuracy, with a multiplicative bias of a few percent in most cases. The flexions displayed a greater bias in general, and a greater sensitivity to the intrinsic brightness profile of the sources. Additionally, the F flexion in particular showed a trend with S/N which may need to be calibrated in lower-quality data.

While the GREAT08 and FLASHES simulation sets were monochromatic, care is needed in future surveys where the PSF may be wavelength-dependent. If a galaxy with an intrinsic colour gradient, such as a redder core and a bluer disk, is observed through a broad filter with an imaging system which results in such a PSF, then there may be additional shear measurement bias induced. With perfect knowledge of the PSF and the intrinsic colour gradient, this may be corrected for but such perfect knowledge is not feasible for surveys such as Euclid. We therefore created simulations based on real galaxies observed in two bands as part of the HST AEGIS survey. Comparing the bias measured in each narrow-band with that measured in a simulated broad-band, we found that the additional bias induced by the galaxy colour gradient was at most at the percentage level, with some variation with redshift, magnitude, size and overall colour. This additional bias may be partly explained by inherent biases in the MV pipeline but the results indicate that it will be possible to accurately determine the magnitude of this effect and thus correct for it. To get a more precise bias estimate we will in the near future create simulations with more realistic intrinsic colour gradients and observe them through several yet narrower bands.

The MV pipeline has been shown here to be both accurate and versatile. We will in the next Chapter apply it to the real COSMOS survey and measure a flexion signal around galaxies for the first time.

Acknowledgements

This study makes use of data from AEGIS, a multiwavelength sky survey conducted with the Chandra, GALEX, Hubble, Keck, CFHT, MMT, Subaru, Palomar, Spitzer, VLA, and other telescopes and supported in part by the NSF, NASA, and the STFC.

The authors would like to thank Gary Bernstein for valuable input and discussions. MV acknowledges support from the European DUEL Research-Training Network (MRTN-CT-2006-036133) and from the Netherlands Organization for Scientific Research (NWO).